

Article

Ce-Doped LaMnO₃ Redox Catalysts for Chemical Looping Oxidative Dehydrogenation of Ethane

Jingwei Wang^{1,2}, Xiaocen Liang^{1,2}, Zifan Xing^{1,2}, Haitao Chen^{1,2}, Yang Li³, Da Song^{1,2}  and Fang He^{1,2,*}¹ College of Chemistry and Bioengineering, Guilin University of Technology, Guilin 541006, China² Guangxi Key Laboratory of Electrochemical and Magneto-Chemical Functional Materials, College of Chemistry and Bioengineering, Guilin University of Technology, Guilin 541004, China³ College of Chemistry and Engineering, Northeast Petroleum University, Daqing 163318, China

* Correspondence: hefang@glut.edu.cn

Abstract: As a novel reaction mode of oxidative dehydrogenation of ethane to ethylene, the chemical looping oxidative dehydrogenation (CL-ODH) of ethane to ethylene has attracted much attention. Instead of using gaseous oxygen, CL-ODH uses lattice oxygen in an oxygen carrier or redox catalyst to facilitate the ODH reaction. In this paper, a perovskite type redox catalyst LaMnO_{3+δ} was used as a substrate, Ce³⁺ with different proportions was introduced into its A site, and its CL-ODH reaction performance for ethane was studied. The results showed that the ratio of Mn⁴⁺/Mn³⁺ on the surface of Ce-modified samples decreased significantly, and the lattice oxygen species in the bulk phase increased; these were the main reasons for improving ethylene selectivity. La_{0.7}Ce_{0.3}MnO₃ showed the best performance during the ODH reaction and showed good stability in twenty redox cycle tests.

Keywords: chemical looping oxidative dehydrogenation; LaMnO₃; Ethane; perovskite type redox catalyst



Citation: Wang, J.; Liang, X.; Xing, Z.; Chen, H.; Li, Y.; Song, D.; He, F. Ce-Doped LaMnO₃ Redox Catalysts for Chemical Looping Oxidative Dehydrogenation of Ethane. *Catalysts* **2023**, *13*, 131. <https://doi.org/10.3390/catal13010131>

Academic Editors: Chuande Huang, Bo Jiang, Xin Tian, Jiawei Hu and Vladimir Sobolev

Received: 27 November 2022

Revised: 28 December 2022

Accepted: 28 December 2022

Published: 6 January 2023



Copyright: © 2023 by the authors. Licensee MDPI, Basel, Switzerland. This article is an open access article distributed under the terms and conditions of the Creative Commons Attribution (CC BY) license (<https://creativecommons.org/licenses/by/4.0/>).

1. Introduction

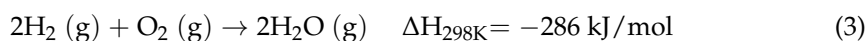
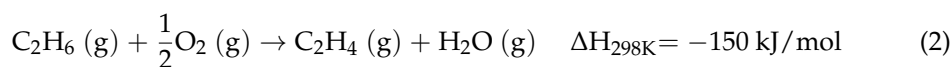
Ethylene is one of the most commonly used feedstocks in the production of numerous chemical intermediates and polymers, and is one of the most produced chemicals in the world [1–3]. The global ethylene market was estimated to be 158 million tons in 2020, and is expected to reach 207.4 million tons in 2027 [4]. At present, steam cracking is mainly carried out by petroleum raw materials, such as petroleum brain and condensate, to achieve ethylene production in industry [5]. Recently, with the increase in shale gas production, there has been extensive attention paid to the use of the underutilized ethane, extracted from shale gas, to produce ethylene [6,7].

In industry, the steam cracking process for ethylene production from ethane is shown in Equation (1) [8]. This reaction is a strongly endothermic reaction with a high reaction temperature (higher than 1000 °C), which inevitably leads to high energy consumption (approximately 16 GJ/[t C₂H₄]), serious carbon deposition, and produces a large number of environmentally unfriendly by-products such as CO₂ (1–1.2 t CO₂/[t C₂H₄]) and NO_x [9,10].



In order to avoid the disadvantages of the traditional steam cracking process, ethylene production via the oxidative dehydrogenation (ODH) of ethane (Equation (2)) is proposed as an alternative method. Compared to steam cracking technology, ODH is an exothermic reaction; therefore, the reaction temperature is lower (300–700 °C), and the energy consumption of tons of ethylene can be reduced by 35%. In addition, due to the participation of gaseous oxygen in the reaction, the hydrogen generated by the cleavage of ethane in the reaction Equation (2) will undergo a combustion reaction (Equation (3)); this can eliminate

the thermodynamic barrier to achieve a high ethane conversion rate and make the reaction kinetics possess lower Gibbs free energy [8,11,12].

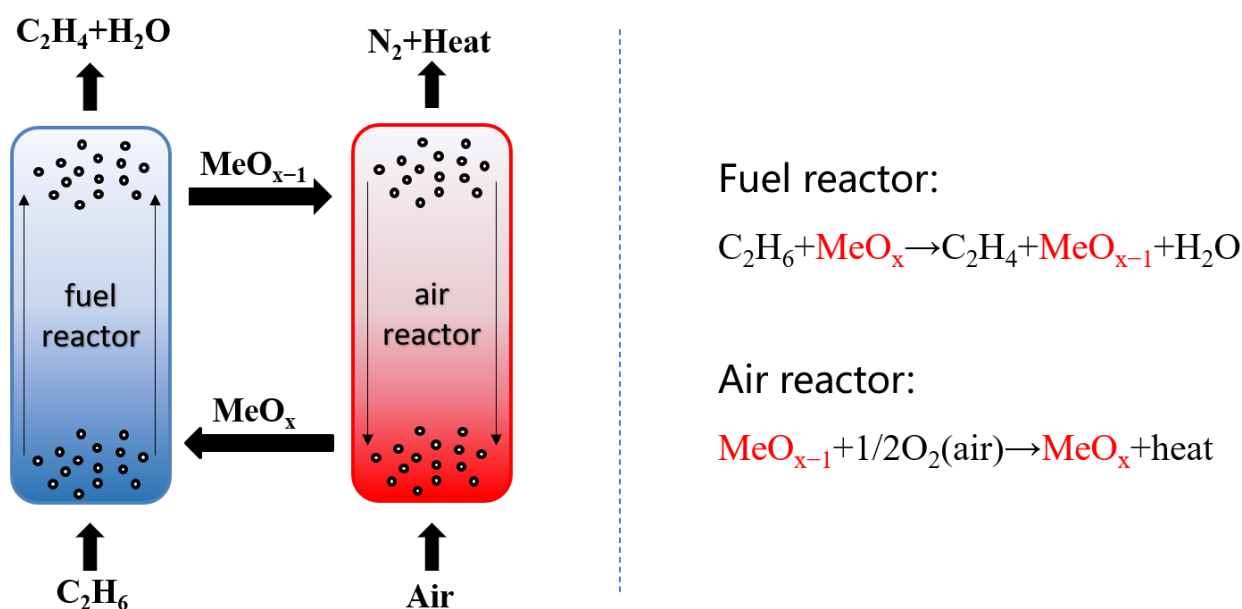


In the past 20 years, a number of ODH catalyst systems have been reported, such as NiO [13], MO-V-O [14], Sn-doped Pt [15], La/Sr/Nd [16], and Mo/V/Te/Nb/O [17]. It has been reported that the ethylene yield of NiO and NiO catalysts, modified with Zr, Ti, Mo, W, and V in the ODH reaction of ethane, ranges from 35% to 38%, among which Ni-W-O and Ni-Ti-O catalysts show the highest ethylene yield [13]. The Mo-V-containing catalysts achieved a high ethylene selectivity of 76% under the condition of 30% ethane conversion [14]. The Mo/V/Te/Nb/O catalyst can achieve 78% ethylene yield [17]. Despite the ODH reaction possessing many potential advantages, it can not replace the steam cracking process in the industry, because there are still some problems that need to be solved; these include the following: (1) In order for pure oxygen or oxygen-enriched air to participate in the ethane ODH reaction, it needs to be in an air separation plant; this no doubt increases the cost of investment and the extent of air separation oxygen in the energy intensive process. (2) The co-feeding of ethane and oxygen has safety hazards. If inert gas is added to dilute the feedstock gas, it will increase the additional costs and bring unnecessary trouble to the separation of subsequent products [18]. (3) With the participation of gas-phase oxygen, the product is more likely to be deeply oxidized to CO_x , which reduces ethylene selectivity [11].

To solve these problems, the chemical looping was combined with the ODH reaction of ethane to form the chemical looping oxidative dehydrogenation of ethane, as shown in Scheme 1 [19–21]. This scheme uses lattice oxygen in an oxygen carrier (also known as a redox catalyst) instead of gas oxygen, to participate in the oxidative dehydrogenation reaction, without needing air separation; thus, the feed mixture of ethane and oxygen is avoided, which inhibits the deep oxidation of the product and minimizes explosion hazards from co-feeding oxygen with ethane. In the CL-ODH scheme, the reaction process between fuel and the oxygen carrier is divided into two steps: In the fuel reactor, ethane is partially oxidized into ethylene by an oxygen carrier (MeO_x); meanwhile, the oxygen carrier is reduced to a reduced state. In the air reactor, the reduced oxygen carrier (MeO_{x-1}) is reoxidized by air to restore its lattice oxygen, completing the redox cycle [22]. Previous studies show that in the chemical looping oxidative dehydrogenation reaction, ethane is firstly cleaved to produce ethylene and hydrogen, and the produced hydrogen is selectively oxidized on the surface of oxygen carrier, breaking the thermodynamic equilibrium and making the reaction go in the direction of ethylene formation [23]. In the ODH reaction, the adsorbed oxygen on the surface of the oxygen carrier will be rapidly consumed to form oxygen vacancies, and the internal lattice oxygen needs to migrate to the surface to fill the oxygen vacancies. Therefore, the lattice oxygen mobility of the oxygen carrier plays a crucial role in the success of the CL-ODH reaction [24]. In the CL-ODH of ethane, the key to this process is to design oxygen carriers with high lattice oxygen mobility, which can selectively burn hydrogen and inhibit the deep oxidation of products.

Recently, perovskite-type oxygen carriers have attracted much attention as redox catalysts due to their unique structure and high stability. The general formula of perovskite-type oxide is ABO_3 , where A is an alkaline earth or rare earth metal cation and B is a transition metal cation. To date, a number of studies have been conducted on the chemical looping oxidative dehydrogenation of ethane using perovskite-type oxygen carriers. In these previous studies, perovskite-type oxides are widely used in chemical looping reactions due to their excellent redox properties and high oxygen mobility. Tian et al. [10] studied that Ce-modified $\text{SrFeO}_{3-\delta}$ achieved up to 29% ethane conversion and 82% ethylene selectivity at 725 °C. In this study, the modification of Ce promoted the formation of surface oxygen vacancies and increased the resistance of lattice oxygen diffusion to the surface, which

was the reason for the increased reactivity and ethylene selectivity. Gao et al. [25] found that the $\text{La}_x\text{Sr}_{2-x}\text{FeO}_{4-\delta}$ catalyst, modified with Li and K, had an ethane conversion of 60% and ethylene selectivity of 86% at 700 °C. It is very important to design and develop efficient redox catalysts to replace gaseous oxygen, inhibit the deep oxidation of ethane, and improve ethylene selectivity for the chemical looping oxidative dehydrogenation of ethane. It was also found that Mn-based oxygen carriers, such as CaMnO_3 , Mg_6MnO_8 , SrMnO_2 , and $\text{Mn}_7\text{SiO}_{12}$, had good performances in the CL-ODH of ethane, and the yield of Mn-based oxygen carriers, modified by Na_2WO_4 , could reach 68.2% [23,24,26–28]. These results indicated that the Mn-based oxygen carrier is a promising oxygen carrier for the oxidative dehydrogenation of ethane. Among the various perovskite-type oxides, LaMnO_3 exhibited a higher thermal stability and better activity, so it is considered to be a more meaningful carrier for the CL-ODH of ethane to produce ethylene [11]. It is generally believed that when different cations are introduced into the A or B sites of perovskite oxides, the lattice structure of perovskite will not change fundamentally, but its reactivity can be improved by regulating the number of oxygen vacancies, regulating the oxygen vacancy symmetry, and oxide lattice distortion [29]. Recently, T. Rajkumar et al. [30] found that in the $\text{CeO}_2/\text{MnO}_x$ system, through the mixing of CeO_2 and MnO_x , the oxidation states of Ce^{3+} and Ce^{4+} in the CeO_2 can be shifted to improve the oxygen vacancy, oxygen mobility and oxygen storage capacity in the lattice; this can change the catalytic activity of the CeO_2 . Therefore, in this paper, by introducing Ce^{3+} cations as heterogeneous ions into the A site of LaMnO_3 to adjust the local chemical environment of the oxygen vacancy, the influence of heterogeneous ions on ethane cleavage and the selective hydrogen burning mechanism in the CL-ODH of ethane were studied. Different proportions of Ce^{3+} were introduced into the A site of the perovskite-type oxide LaMnO_3 to carry out the CL-ODH reaction. The doping of Ce^{3+} can form asymmetric oxygen vacancies (some studies have shown that asymmetric oxygen vacancies easily adsorb oxygen in an oxidizing atmosphere, and desorb oxygen in a reducing atmosphere), actively regulate the local chemical environment of lattice oxygen and oxygen vacancies, and achieve the effect of increasing ethylene selectivity [29].



Scheme 1. A schematic view for the concept of ethane CL-ODH.

2. Results and Discussions

2.1. Structural Characterization

The lattice structure, crystal size and lattice parameters of the prepared LMO, 0.1LCMO, 0.2LCMO, 0.3LCMO and 0.4LCMO samples were characterized by XRD; the results are shown in Figure 1 and Table 1. The appearance of a peak indicates a good crystallinity.

For the samples without Ce doping, there was no secondary phase. According to the JCPDS card (PDF # 82-1152), the sample shows the characteristic peaks of a hexagonal LaMnO_3 phase. The main peaks are at $2\theta = 21.69^\circ, 31.25^\circ, 31.57^\circ, 38.87^\circ, 45.54^\circ$ and 56.8° , corresponding to (012), (110), (104), (202), (024), and (214) planes, respectively. When Ce is doped into LaMnO_3 , there will be a second phase, and an orthorhombic perovskite is formed. The secondary phase has a main peak at 2θ of $27.34^\circ, 31.88^\circ, 46.22^\circ$ and 55.12° , which is assigned to the CeO_2 (PDF # 89-8436) phase. Moreover, it can be clearly observed that with the gradual increase in the Ce doping amount, the characteristic peak intensity of the parent LaMnO_3 gradually weakens, while the peak intensity of the CeO_2 gradually increases [31]. The presence of the CeO_2 phase was attributed to the surface enrichment of atomic cerium and it not being incorporated into the LaMnO_3 perovskite framework during the calcination process. Therefore, the $\text{La}_{1-x}\text{Ce}_x\text{MnO}_{3+\delta}$ samples were considered to be multiple oxides, containing Ce-doped perovskite and cerium oxide [32]. The lattice structure, crystal size and lattice parameters of each sample are listed in Table 1. It can be seen that the total crystal size of $\text{La}_{1-x}\text{Ce}_x\text{MnO}_{3+\delta}$ samples was smaller than that of $\text{LaMnO}_{3+\delta}$, indicating that the doping of Ce degraded the crystallinity of perovskite crystal. The lattice parameters of $\text{La}_{1-x}\text{Ce}_x\text{MnO}_{3+\delta}$ decreased due to Ce doping. The lattice shrinks of $\text{La}_{1-x}\text{Ce}_x\text{MnO}_{3+\delta}$ crystal were attributed to the substitution of La^{3+} (ionic radii is 1.032 \AA) by Ce^{3+} (ionic radii is 1.02 \AA), though there is a certain amount of Ce^{4+} (ionic radii is 0.87 \AA) in the $\text{La}_{1-x}\text{Ce}_x\text{MnO}_{3+\delta}$ perovskite [33].

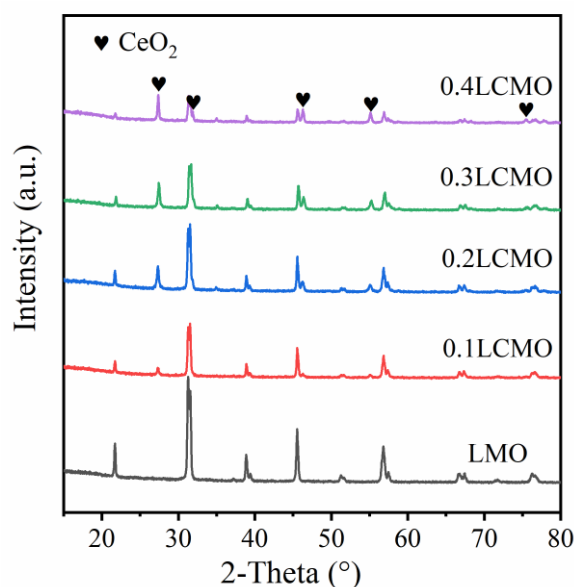


Figure 1. XRD patterns of as-prepared redox catalysts.

Table 1. Lattice structure, crystal size and lattice parameters of each fresh sample.

Samples	Lattice Structure	Crystal Size (nm)	a (Å)	b (Å)	c (Å)	Vol (Å ³)
LMO	hexagonal	21.93	5.525	5.525	13.361	407.853
0.1LCMO	orthorhombic	21.02	5.517	5.517	13.356	406.530
0.2LCMO	orthorhombic	19.56	5.516	5.516	13.348	406.130
0.3LCMO	orthorhombic	19.15	5.517	5.517	13.351	406.368
0.4LCMO	orthorhombic	18.23	5.521	5.521	13.358	407.171

In order to observe the micromorphology and element distribution of the samples more intuitively, the fresh samples were characterized by SEM-EDS, as shown in Figures 2 and 3. It can be clearly seen that all samples have a similar porous structure, and all elements are uniformly dispersed in the prepared samples. From the results of the BET experiment,

as shown in Table 2, the specific surface area of the samples is between 3.1–5.1 m²/g, and the specific surface area of LaMnO₃ without Ce doping is the smallest.

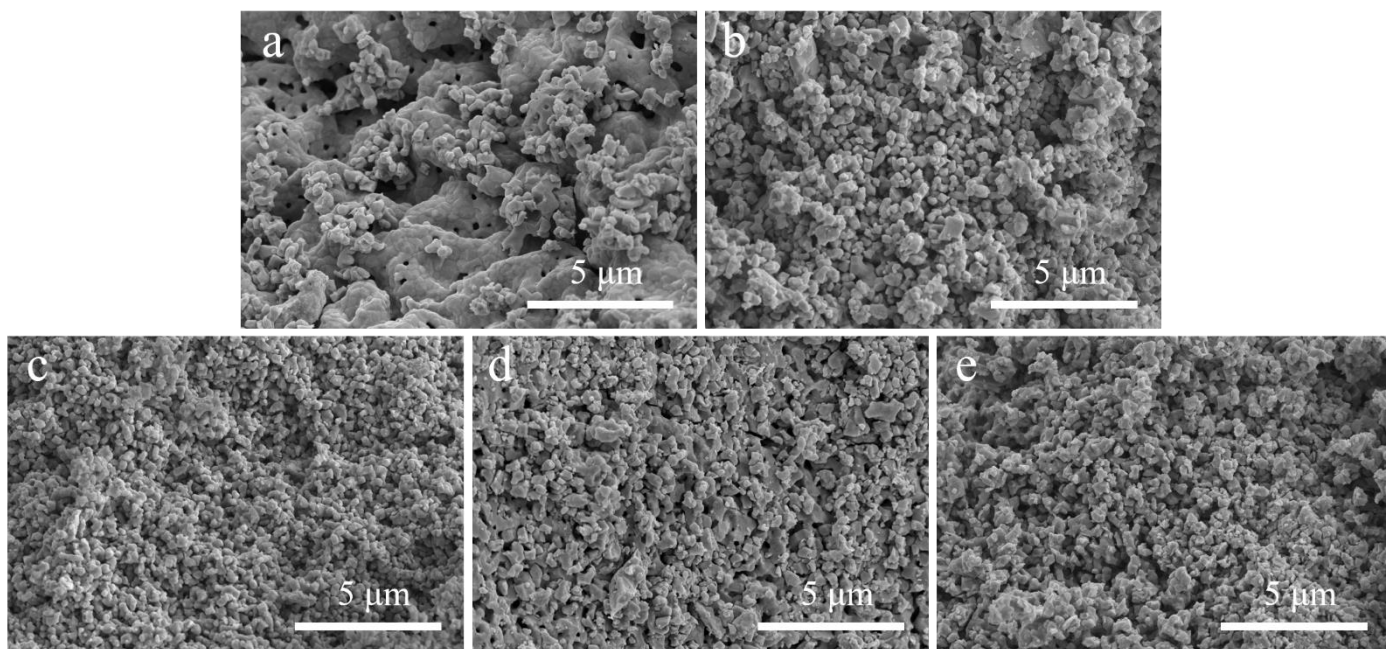


Figure 2. SEM images of fresh LMO (a), 0.1LCMO (b), 0.2LCMO (c), 0.3LCMO (d), 0.4LCMO (e).

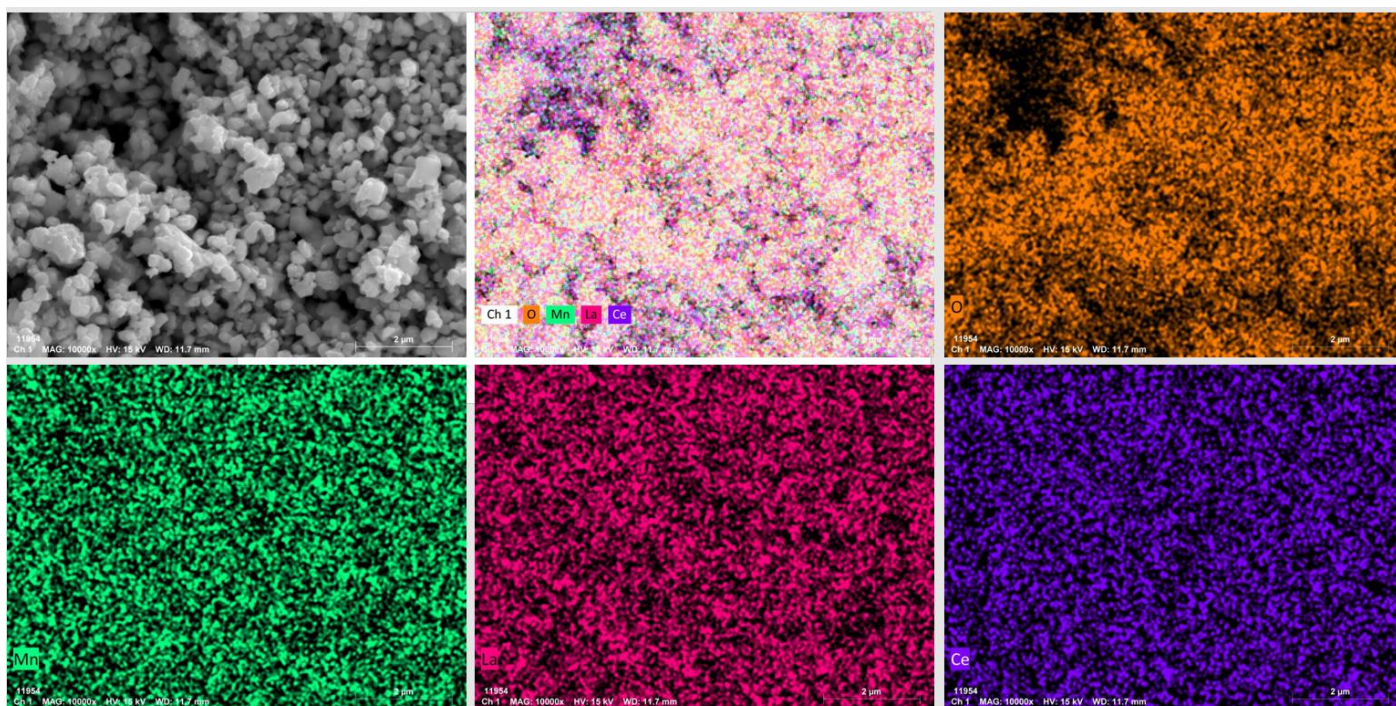


Figure 3. EDS spectra of fresh 0.3LCMO.

2.2. XPS

In order to further explore the influence of Ce-doping on the performance of LaMnO₃ in ODH reactions of ethane, XPS technology was used to test the types of manganese ions and oxygen species near the surface of the oxygen carrier. It is known that the manganese ions, located in the B sites of perovskite, directly affect the reactivity of perovskite;

meanwhile, the properties of the near-surface oxygen species greatly affect the ethylene selectivity of oxygen carriers for ethane conversion. Therefore, the O 1s and Mn 2p spectra of each sample were analyzed in detail, and the results are shown in Figure 4.

Table 2. Structural information of the fresh catalysts.

	S_{BET} (m ² /g)	V_{pore} (cm ³ /g)	Average Pore Diameter (nm)
LCMO	3.1	0.01	9.2
0.1LCMO	5.1	0.02	14.7
0.2LCMO	3.4	0.02	17.1
0.3LCMO	4.7	0.04	26.4
0.4LCMO	5.0	0.03	15.8

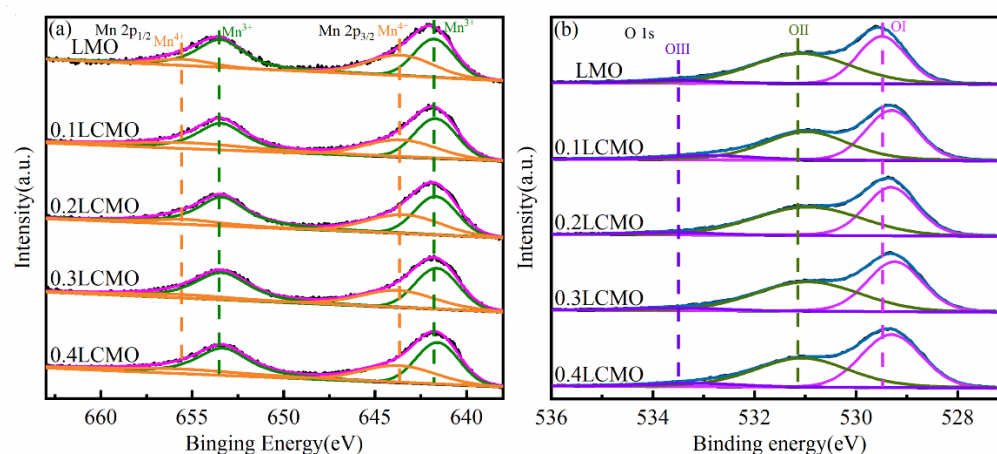


Figure 4. XPS spectra for (a) and (b) of the fresh samples.

As shown in Figure 4a, the Mn 2p is featured with a double-peaked spectrum, assigned to Mn 2p_{1/2} and Mn 2p_{3/2}, respectively, due to energy level splitting. For each sample, two peaks with binding energies of around 641.5~641.8 eV and 643.4~643.8 eV were obtained via the deconvolution of Mn 2p_{3/2} spectra, corresponding to Mn³⁺ and Mn⁴⁺ species, respectively [34–36]. This is consistent with the analysis of the binding energy location of Mn³⁺ and Mn⁴⁺ species in Yin et al.'s study [34]. According to the detailed data of Mn 2p_{3/2} shown in Table 3, as Ce is introduced into the oxygen carrier, the characteristic peak of manganese shows a trend reflecting a transfer from a high binding energy to a low binding energy, and the value of Mn⁴⁺/Mn³⁺ is obviously reduced. Considering the potential incorporation of Ce⁴⁺ with a higher valence than La³⁺, which causes the distortion of the perovskite structure and the imbalance of internal charges, it is necessary to compensate by converting Mn⁴⁺ into Mn³⁺, so more active sites are generated and more oxygen vacancies are formed [10]. Combined with the CL-ODH results, the changing trend in ethylene selectivity is negatively correlated with the changing trend in Mn⁴⁺/Mn³⁺ value, indicating that the formation of Mn³⁺ is conducive to the selective production of ethylene from ethane.

Table 3. Molar proportion of surface element for each fresh sample was measured by XPS.

	Mn 2p _{3/2}			O 1s			
	Mn ³⁺	Mn ⁴⁺	Mn ⁴⁺ /Mn ³⁺	OI	OII	OIII	OI/(OII+OIII)
LCMO	0.53	0.47	0.90	0.40	0.55	0.05	0.67
0.1LCMO	0.58	0.42	0.74	0.47	0.44	0.09	0.88
0.2LCMO	0.54	0.46	0.85	0.45	0.52	0.03	0.81
0.3LCMO	0.55	0.45	0.81	0.46	0.50	0.04	0.85
0.4LCMO	0.58	0.42	0.71	0.49	0.46	0.05	0.96

For the deconvolution of O 1s spectrum, two main peaks and one secondary peak can be observed in all samples; these are the lattice oxygen species (O^{2-} , O I) near 529.2~529.5 eV, surface electrophilic oxygen species (O II) near 530.9~531.1 eV and the hydroxide/carbonate species (OH^-/CO_3^{2-} , O III) near 533.1~533.9 eV [37,38]. It is generally believed that both lattice oxygen and surface electrophilic oxygen species can improve the conversion rate of ethane in CL-ODH reactions. The difference is that lattice oxygen can promote the selective conversion of ethane to ethylene, whereas the electrophilic oxygen species is usually non-selective and prone to causing the deep oxidation of ethane [24,28]. It can be seen from the O 1s in Figure 4b, and the data in Table 3, that the relative content of the lattice oxygen of $LaMnO_3$ is obviously less than that of the doped sample, consistent with its worst selectivity in the CL-ODH process. The higher proportion of the lattice oxygen species in 0.1LCMO and 0.4LCMO is consistent with their relatively high ethane selectivity. As far as 0.2LCMO and 0.3LCMO are concerned, due to the similar relative amount of active oxygen substances (i.e., lattice oxygen and surface electrophilic oxygen), their reaction activities are almost the same (97% vs. 96%). As for the 0.3LCMO sample, it has a higher proportion of lattice oxygen, thereby giving a better reaction performance in CL-ODH.

2.3. H_2 -TPR and O_2 -TPD

In order to understand the reducibility of oxygen carriers in the CL-ODH reaction, a H_2 -TPR test was conducted, and the H_2 -TPR curve of the sample is shown in Figure 5a. It can be observed that all samples have two obvious reduction peaks, which are located at 300–620 °C and 650–850 °C, respectively. The reduction peak at low temperatures may originate from the consumption of adsorbed oxygen on the surface and the reduction of Mn^{4+} to Mn^{3+} , while the reduction peak at high temperatures is corresponding to the removal of lattice oxygen from the reduction of Mn^{3+} to Mn^{2+} [34,39]. It can be observed that the initial reduction peak position of the modified oxygen carrier obviously moves to the lower temperature, indicating that the addition of Ce improves the oxygen mobility of $LaMnO_3$ and the reducibility of the sample. It is generally believed that the samples with high reducibility have higher activity, which is consistent with the CL-ODH reaction results [25].

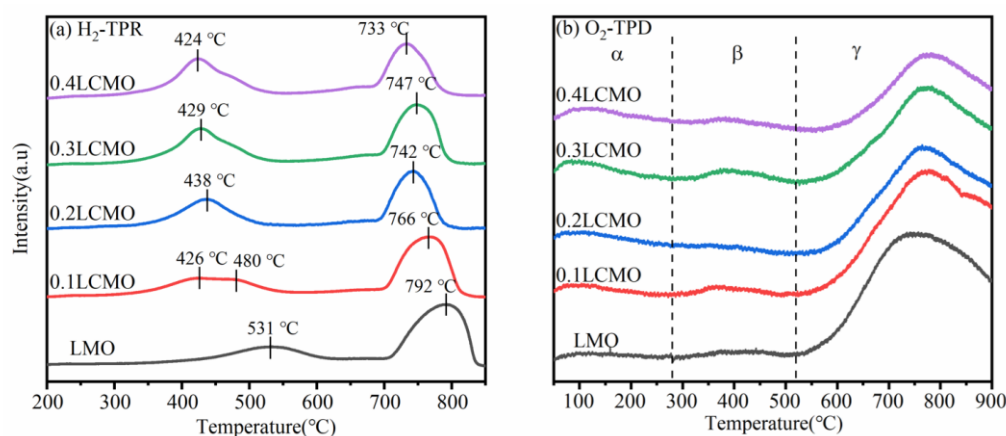


Figure 5. Results of the oxygen carriers.

In order to study the relative amounts of various oxygen species in the oxygen carrier, an O_2 -TPD test was conducted on the fresh oxygen carrier. Figure 5b shows the O_2 -TPD curve for each sample. According to the previous literature published to date, the curve is usually divided into three peaks, labeled as α , β and γ [40,41]. The α peak is in the temperature range below 280 °C, and the appearance of this decomposition absorption peak is attributed to the desorption of surface chemisorbed oxygen (O_2^- , O_2^{2-} , O^-). The β desorption peak, in the range of 280 °C–520 °C, is caused by the surface lattice oxygen

(O^{2-}) species. The higher temperature range of γ is related to the bulk lattice oxygen of perovskite crystals [40–43]. It can be noticed that the peaks in the α and β regions of the doped samples have significant changes, especially for the sample 0.3LCMO; this gives a significantly enhanced β peak region, which indicates that the introduction of cerium is conducive to the formation of more oxygen vacancies and improves the sample oxygen mobility. At elevated temperatures, it can be seen that the peak value of the γ region is shifted to a higher temperature due to the doping of cerium, which indicates that the oxidation activity of modified samples is worse at high temperatures. Therefore, the modification of the $LaMnO_3$ substrate is more conducive to the optimization of the reaction performance at low temperatures.

2.4. Ethane CL-ODH Reaction Resting

In the continuous cycle pulse experiment, due to the existence of adsorbed oxygen on the surface of the oxygen carrier, non-selective oxidation may occur at the beginning of the pulse, resulting in the poor performance of the sample. The continuous pulse experiment results of the 0.2LCMO sample at 700 °C are shown in Figure 6. It can be observed that in the first two pulses, the non selective oxygen species are rapidly consumed, and the sample performance tends to be stable without too much negative impact [44]. The ethane conversion, ethylene selectivity and ethylene yield data of different samples obtained in the CL-ODH step, at various temperatures (650 °C, 675 °C and 700 °C), are shown in Figure 7. The carbon balance calculations for all tests were in the range of 93102%. Perovskite-type oxygen carriers exhibit a satisfactory redox performance in the CL-ODH reaction at 700 °C. It can be seen from Figure 7c that, compared with the oxygen carrier without Ce, the reactivity of the modified oxygen carrier was almost improved, and it obtained a higher ethylene selectivity. These results show that the introduction of Ce is effective in improving the CL-ODH reaction performance of the $LaMnO_3$ substrate. Among all oxygen carriers, 0.3LCMO exhibited the highest activity for ethane conversion and moderate ethylene selectivity. While 0.1LCMO had a higher ethylene selectivity, the activity was the worst. Once the Ce-doping content was above 0.3, the activity or ethylene selectivity of the Ce-doped samples was further improved with the Ce content. Therefore, 0.3LCMO is considered to have the most suitable Ce doping ratio.

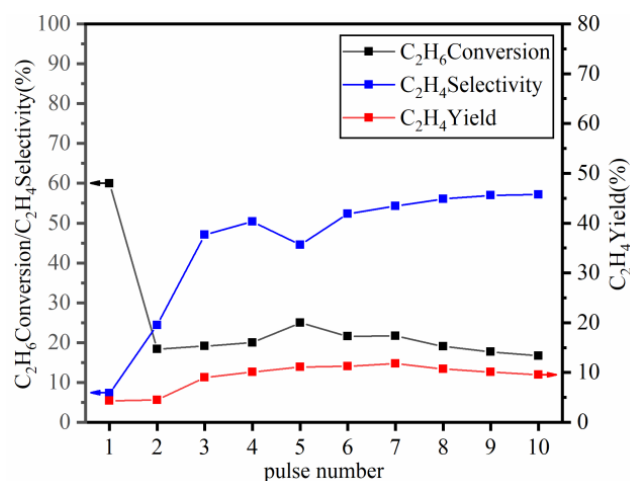


Figure 6. The 0.2LCMO continuous pulse experiment at 700 °C (GHSV = 1200 mL/h·g).

2.5. Cyclic Stability

The excellent stability and recyclability of perovskite-type catalysts at high temperatures are critical for multiple redox cycles in the utilization of chemical looping. Therefore, the 0.3LCMO sample with the best reaction performance was subjected to 20 consecutive cycles of redox tests, and the reaction results are shown in Figure 8. In the ethane ODH step,

the conversion of ethane fluctuated slightly between 35–40%, while ethylene selectivity remained in the range of 25–30%, and the yield did not decline significantly after 20 cycles. The XRD results (Figure 9) can further confirm the structural stability of the 0.3LCMO sample. The sample after the re-oxidation cycle obtained the same XRD patterns as the fresh sample, and the characteristic peaks after successive redox cycles were dominated by LaMnO_3 characteristic peaks. In addition, it is noted that the sample showed weak peaks at $2\theta = 34.9^\circ$ and $2\theta = 40.5^\circ$ after cycling, which corresponded to MnO [34]. The SEM-EDS results (Figures 10 and 11) show that the structure of the circulating sample remains good after the cycle, and all elements are evenly distributed in the oxygen carrier.

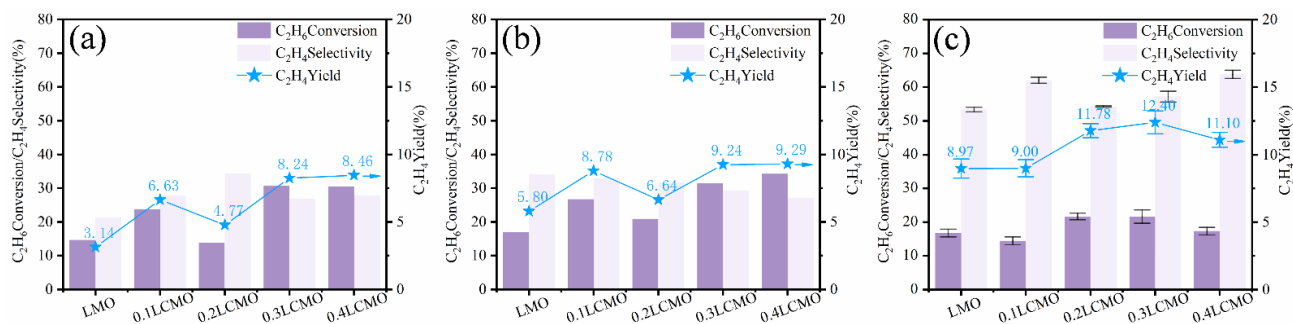


Figure 7. The ethane ODH reaction performances of different oxygen carriers at (a) 650 °C, (b) 675 °C and (c) 700 °C (GHSV = 1200 mL/h·g).

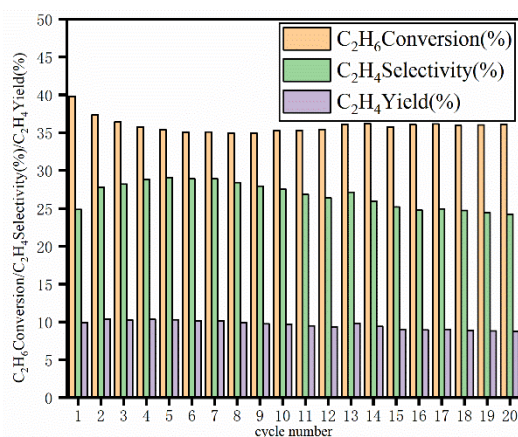


Figure 8. CL-ODH cycle for 0.3LCMO redox catalyst (GHSV = 1200 mL/h·g).

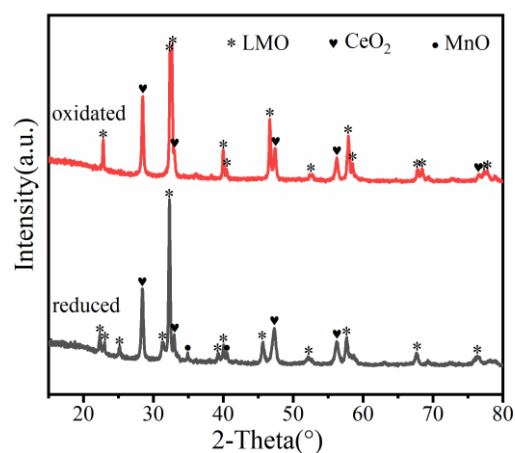


Figure 9. XRD patterns of 0.3LCMO after 20 continuous cycles test and regeneration.

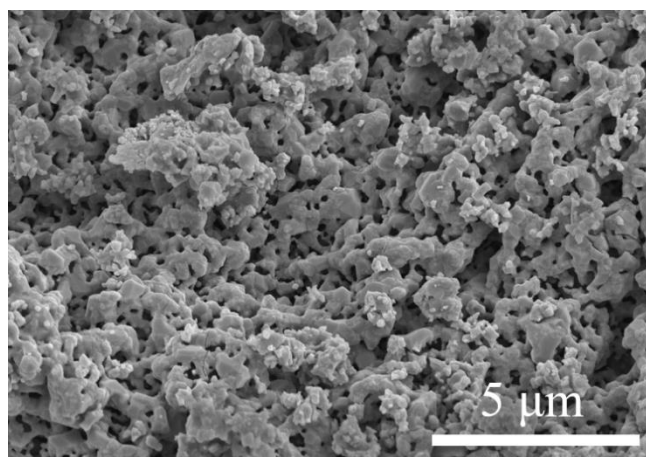


Figure 10. SEM images of 0.3LCMO after circulation.

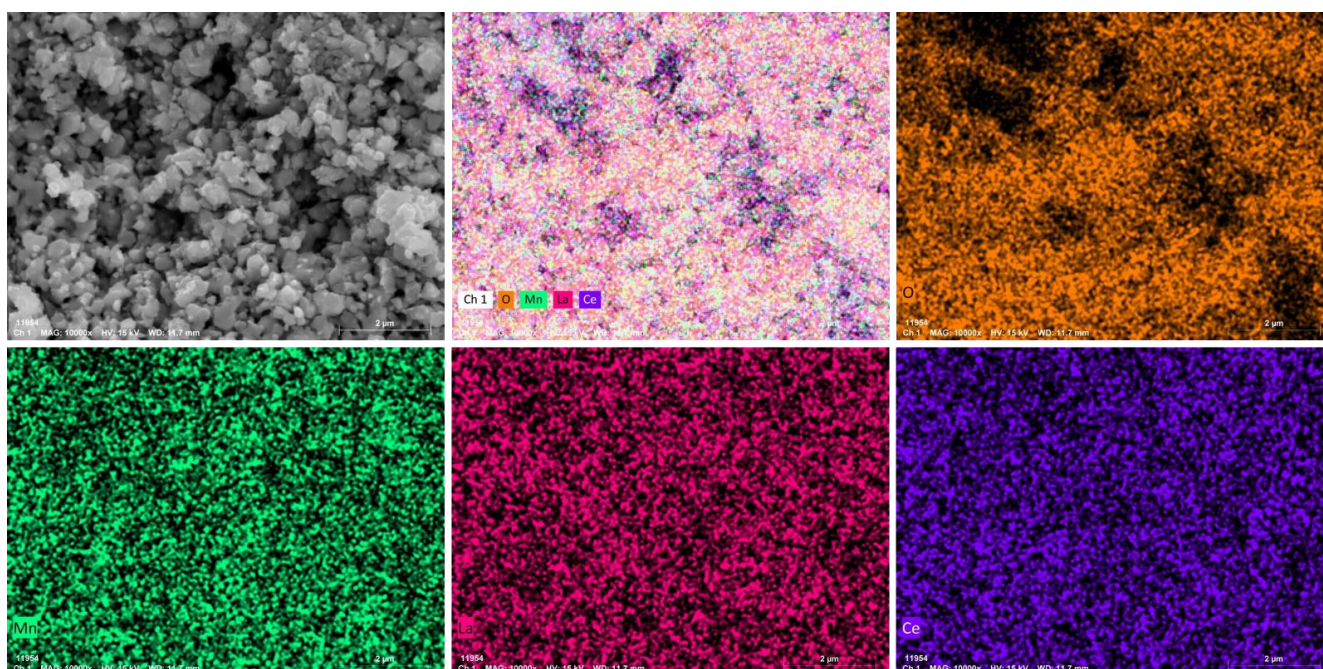


Figure 11. EDS spectra of 0.3LCMO after circulation.

3. Experimental Section

3.1. Redox catalyst Preparation

The $\text{La}_{1-x}\text{Ce}_x\text{MnO}_{3+\delta}$ ($x = 0, 0.1, 0.2, 0.3, 0.4$) oxygen carriers used in this work were all prepared by a simple sol-gel method described elsewhere [45–48]. Firstly, $\text{La}(\text{NO}_3)_3 \cdot 6\text{H}_2\text{O}$ (Aladdin, 99.99% purity), $\text{Ce}(\text{NO}_3)_3 \cdot 6\text{H}_2\text{O}$ (Aladdin, 99.95% purity) and $\text{Mn}(\text{NO}_3)_2$ (Rhawn, 50 wt.% in solution) were dissolved in deionized water with a certain molar ratio (e.g. $\text{La}_{0.9}\text{Ce}_{0.1}\text{MnO}_{3+\delta}$, $\text{La}(\text{NO}_3)_3 \cdot 6\text{H}_2\text{O} : \text{Ce}(\text{NO}_3)_3 \cdot 6\text{H}_2\text{O} : \text{Mn}(\text{NO}_3)_2 = 0.9:0.1:1$), and the total nitrate concentration reached 1 mol/L. Then citric acid ($\text{C}_6\text{H}_8\text{O}_7 \cdot \text{H}_2\text{O}$, Aladdin, $\geq 99.5\%$ purity) was added to the solution, and the molar ratio of citric acid to total nitrate ions was 3:1. After the mixture was stirred in a water bath at 60°C for 30 min, glycol solution ($\text{C}_2\text{H}_6\text{O}_2$, Aladdin, $\geq 99.5\%$ purity) was added, and the molar ratio of glycol solution to citric acid was 2:1. The solution was heated to 80°C under constant stirring (approximately 24 h) until a sol-like viscous substance formed. The gel was dried in a blast drying oven at 120°C for 24 h. Finally, the sample was decomposed at 350°C for 2 h and then calcinated at 1000°C for 8 h in a muffle furnace; the heating rate of the calcination was $10^\circ\text{C}/\text{min}$.

Eventually, five samples were attained, and they were labeled as LMO, 0.1LCMO, 0.2LCMO, 0.3LCMO, and 0.4LCMO, respectively. All samples were ground and sieved into the size range of 0.45–0.9 mm for reaction testing.

3.2. CL-ODH Experiments

The reaction performance of ethane CL-ODH was tested in a micro fixed-bed quartz tube reactor under atmospheric pressure; the length of the catalyst bed was 300 mm. In this experiment, the length of the quartz tube was 440 mm, the outer diameter was 8 mm, and the inner diameter was 6 mm. The amount of redox catalyst was 1.5 g. The appropriate amount of quartz wool was used to fix the catalyst on its upper and lower sides, but also to reduce the gas flow in the heated reaction area.

The whole fixed-bed reaction was divided into two stages: reduction and oxidation. In the reduction stage, the fixed-bed reactor acted as a fuel reactor and was heated to the reduction temperature in pure argon at 10 °C/min. Then, the atmosphere was switched to 40% ethane/balance nitrogen, and the air flow rate was 30 mL/min. After that, the argon gas was blown at the same speed and gas bags were used to collect all the tail gas at this stage. Next was the oxidation stage; here, the fixed-bed reactor acted as an air reactor, using 21% oxygen/balanced nitrogen to oxidize the catalyst; argon was also used for line purging.

Before the performance test, in order to explore the potential oxygen capacity of the prepared oxygen carrier, a continuous pulse experiment was carried out. After the reactor was filled with reaction gas (40% ethane/balance nitrogen) for 1 min, it was purged with argon for 2 min to complete a single pulse. Then, it was pulsed ten times continuously to observe the best performance time. All samples adopted the performance data at the same time. Each experiment was repeated three times.

In order to test the cycle stability of the materials, redox cycle experiments were carried out for the materials with the best performance. The reaction temperature was set to 700 °C, reaction gas was injected for 1 min in the reduction phase, and it was purged with argon for 2 min. Then, 21% O₂ (N₂ as balance gas) was used in the oxidation stage, and the flow rate was 20 mL/min for 4 min. The reactor was purged for 4 min by 30 mL/min argon between each redox cycle.

A Shimadzu GC-2014 gas chromatograph equipped with a flame ionization detector (FID, for hydrocarbon analysis) and two thermal conductivity detectors (TCD, for CO/CO₂ and H₂ analysis, respectively) was used to test the exhaust of the phone. According to the carbon balance, the C₂H₆ conversion, C₂H₄ selectivity, and C₂H₄ yield can be calculated using the following formulas:

$$\text{Conversion of ethane(\%)} = \frac{\text{introduced ethane} - \text{residual ethane}}{\text{introduced ethane}} \times 100\% \quad (4)$$

$$\text{Selectivity of ethylene(\%)} = \frac{\text{produced ethylene}}{\text{converted ethane}} \times 100\% \quad (5)$$

$$\text{Yield of ethylene(\%)} = \frac{\text{produced ethylene}}{\text{introduced ethane}} \times 100\% \quad (6)$$

3.3. Characterization Techniques

X-ray diffraction (XRD) was used to analyze the crystal structure of the samples. The test conditions were the following: Cu K α radiation, a wavelength of $\lambda = 1.5406 \text{ \AA}$, a scanning speed of 15°/min, a target voltage of 40 kV, a target current of 40 mA, and a scanning angle of 15–80°. The specific surface area of the catalyst was measured by the JW-BK112 automatic physical adsorption analyzer using the Brunauer Emmett Teller (BET) theory. Before the test, the samples were dried in a vacuum at 300 °C for 3 h to completely remove the adsorbed water vapor and other impurities. Then, the pretreated samples were tested at low temperatures with liquid nitrogen (−196 °C) to obtain the adsorption and analytical curves. SU-5000 field emission scanning electron microscopy (SEM) was used to

observe the microstructure of the catalyst under the conditions of 3 kV accelerating voltage and 5 mm working distance. At the same time, an XFlash6110 energy-dispersive spectrum analyzer (EDS) was used to analyze the element content of the catalyst. It is worth noting that in an SEM test, the sample needs to be treated with gold spraying before observation.

A hydrogen temperature programmed reduction (H_2 -TPR) experiment was performed, using a PCA-1200 full-automatic temperature program of Beijing Builder Electronic Technology Company. First, the sample (0.01~0.015 g) was heated to 300 °C at 10 °C/min under 30 mL/min nitrogen atmosphere and kept constant for 1 h to remove moisture and adsorbed gas, and then cooled to room temperature naturally. In the reduction process, 5% H_2 /Ar gas (the gas flow rate is 30 mL/min) was used and the temperature was increased to 900 °C (the heating rate was 10 °C/min) to obtain the H_2 -TPR curve. Oxygen temperature programmed desorption (O_2 -TPD) experiments were carried out using the same chemisorption instrument; in this experiment, the sample quantity was 0.1~0.15 g, and the gas flow rate of the gas used was 30 mL/min. The pretreatment process of the samples was the same as that of the H_2 -TPR experiment. After that, the pretreated samples were adsorbed in a pure oxygen environment for 1 h at 60 °C, and then switched to a helium atmosphere. After the TCD signal was stable, the temperature rate was increased to 900 °C at 10 °C/min, and signal data were recorded. The X-ray photoelectron spectroscopy (XPS) test used the ESCALAB 250 Xi multifunctional and high-performance surface analyzer of the US Thermo-Fisher Scientific Company. The experimental conditions were Al $K\alpha$ rays ($h\nu = 1486.6$ eV) as the excitation source, and a power of 150 W. With channel energies of 20 eV and 100 eV, the total spectrum and the single element spectrum of C, La, Mn, Ce and O were obtained, respectively.

4. Conclusions

In this study, $LaMnO_3$ redox catalysts, modified with different proportions of cerium, were prepared by the sol-gel method for the CL-ODH reaction of ethane. Their properties were characterized by XRD, SEM, BET, XPS, H_2 -TPR, O_2 -TPD, etc. XRD shows that a CeO_2 phase is formed in Ce doped $LaMnO_3$, and the introduction of Ce^{4+} will cause the lattice distortion of calcium titanium. From the XPS results, it can be concluded that Ce^{4+} will promote the conversion of Mn^{4+} to Mn^{3+} , which is conducive to improving the ethylene conversion rate. The increase in active oxygen species plays a positive role in the reaction activity of the samples. Among all the catalysts, 0.3LCMO showed the best performance in the ODH reaction process, obtaining a 22% ethane conversion and 57% ethylene selectivity; this was improved compared with the substrate $LaMnO_3$, and showed a higher stability in the redox cycle experiment. This study makes a new attempt to further the design and development of perovskite-type redox catalysts; it also lays a foundation for the development of high-performance oxygen carriers for the ethane CL-ODH reaction.

Author Contributions: Conceptualization, J.W. and X.L.; methodology, J.W.; software, J.W.; validation, J.W., X.L. and F.H.; formal analysis, Z.X. and F.H.; investigation, J.W.; resources, H.C.; data curation, J.W.; writing—original draft preparation, J.W.; writing—review and editing, D.S. and F.H.; visualization, Y.L.; supervision, X.L. and D.S.; project administration, Y.L.; funding acquisition, F.H. All authors have read and agreed to the published version of the manuscript.

Funding: The authors gratefully acknowledge the financial support from the National Natural Science Foundation of China (22179027), Guangxi Natural Science Foundation (2018GXNSFDA281005, 2021GXNSFAA075036).

Data Availability Statement: Not applicable.

Conflicts of Interest: The authors declare no conflict of interest.

References

1. Dai, Y.H.; Gao, X.; Wang, Q.; Wan, X.Y.; Zhou, C.M.; Yang, Y.H. Recent Progress in Heterogeneous Metal and Metal Oxide Catalysts for Direct Dehydrogenation of Ethane and Propane. *Chem. Soc. Rev.* **2021**, *50*, 5590–5630. [[CrossRef](#)] [[PubMed](#)]
2. Mishanin, I.I.; Bogdan, T.V.; Koklin, A.E.; Bogdan, V.I. Design of Highly Selective Heterogeneous Catalyst for CO₂-mediated Ethane Oxidative Dehydrogenation Based on Nonoxidative Catalysis in Stainless-steel Reactor. *Chem. Eng. J.* **2022**, *446*, 137184. [[CrossRef](#)]
3. Najari, S.; Saeidi, S.; Concepcion, P.; Dionysiou, D.D.; Bhargava, S.K.; Lee, A.F.; Wilson, K. Oxidative Dehydrogenation of Ethane: Catalytic and Mechanistic Aspects and Future Trends. *Chem. Soc. Rev.* **2021**, *50*, 4564–4605. [[CrossRef](#)] [[PubMed](#)]
4. Tian, Y.; Westmoreland, P.R.; Li, F.X. CaMn_{0.9}Ti_{0.1}O₃ Based Redox Catalysts for Chemical Looping-Oxidative Dehydrogenation of Ethane: Effects of Na₂MoO₄ Promoter and Degree of Reduction on the Reaction Kinetics. *Catal. Today* **2022**. [[CrossRef](#)]
5. Amghizar, I.; Vandewalle, L.A.; Van Geem, K.M.; Marin, G.B. New Trends in Olefin Production. *Engineering* **2017**, *3*, 171–178. [[CrossRef](#)]
6. Sattler, J.J.H.B.; Ruiz-Martinez, J.; Santillan-Jimenez, E.; Weckhuysen, B.M. Catalytic Dehydrogenation of Light Alkanes on Metals and Metal Oxides. *Chem. Rev.* **2014**, *114*, 10613–10653. [[CrossRef](#)]
7. Zhang, R.H.; Wang, H.; Tang, S.Y.; Liu, C.J.; Dong, F.; Yue, H.R.; Liang, B. Photocatalytic Oxidative Dehydrogenation of Ethane Using CO₂ as a Soft Oxidant over Pd/TiO₂ Catalysts to C₂H₄ and Syngas. *ACS Catal.* **2018**, *8*, 9280–9286. [[CrossRef](#)]
8. Luongo, c.; Donat, F.; Krödel, M.; Cormos, C.; Müller, C.R. Experimental Data Supported Techno-economic Assessment of the Oxidative Dehydrogenation of Ethane through Chemical Looping with Oxygen Uncoupling. *Renew. Sust. Energ. Rev.* **2021**, *149*, 111403. [[CrossRef](#)]
9. Neal, L.M.; Yusuf, S.; Sofranko, J.A.; Li, F.X. Oxidative Dehydrogenation of Ethane: A Chemical Looping Approach. *Energy Technol.* **2016**, *4*, 1200–1208. [[CrossRef](#)]
10. Tian, X.; Zheng, C.H.; Zhao, H.B. Ce-modified SrFeO_{3-δ} for Ethane Oxidative Dehydrogenation Coupled with CO₂ Splitting via a Chemical Looping Scheme. *Appl. Catal. B-Environ.* **2022**, *303*, 120894. [[CrossRef](#)]
11. Ding, W.X.; Zhao, K.; Jiang, S.C.; Zhao, Z.L.; Cao, Y.; He, F. Alkali-metal Enhanced LaMnO₃ Perovskite Oxides for Chemical Looping Oxidative Dehydrogenation of Ethane. *Appl. Catal. A-Gen.* **2021**, *609*, 117910. [[CrossRef](#)]
12. Maffia, G.J.; Gaffney, A.M.; Mason, O.M. Techno-Economic Analysis of Oxidative Dehydrogenation Options. *Top. Catal.* **2016**, *59*, 1573–1579. [[CrossRef](#)]
13. Zhu, H.B.; Dong, H.L.; Laveille, P.; Saih, Y.; Caps, V.; Basset, J. Metal Oxides Modified NiO Catalysts for Oxidative Dehydrogenation of Ethane to Ethylene. *Catal. Today* **2014**, *228*, 58–64. [[CrossRef](#)]
14. Solsona, B.; Dejoz, A.; Garcia, T.; Concepción, P.; Lopez Nieto, J.M.; Vázquez, M.I.; Navarro, M.T. Molybdenum–vanadium Supported on Mesoporous Alumina Catalysts for the Oxidative Dehydrogenation of Ethane. *Catal. Today* **2006**, *117*, 228–233. [[CrossRef](#)]
15. Yokoyama, C.; Bharadwaj, S.S.; Schmidt, L.D. Platinum-tin and Platinum-copper Catalysts for Autothermal Oxidative Dehydrogenation of Ethane to Ethylene. *Catal. Lett.* **1996**, *38*, 181–188. [[CrossRef](#)]
16. Dai, H.X.; Ng, C.F.; Au, C.T. Perovskite-Type Halo-oxide La_{1-x}Sr_xFeO_{3-δ}X_σ (X=F, Cl) Catalysts Selective for the Oxidation of Ethane to Ethene. *J. Catal.* **2000**, *189*, 52–62. [[CrossRef](#)]
17. Védrine, J.C.; Fehete, I. Heterogeneous Partial Oxidation Catalysis on Metal Oxides. *CR Chim.* **2016**, *19*, 1203–1225. [[CrossRef](#)]
18. Baroi, C.; Gaffney, A.M.; Fushimi, R. Process Economics and Safety Considerations for the Oxidative Dehydrogenation of Ethane Using the M1 Catalyst. *Catal. Today* **2017**, *298*, 138–144. [[CrossRef](#)]
19. Mendiara, T.; García-Labiano, F.; Abad, A.; Gayán, P.; de Diego, L.F.; Izquierdo, M.T.; Adánez, J. Negative CO₂ Emissions through the Use of Biofuels in Chemical Looping Technology: A Review. *Appl. Energ.* **2018**, *232*, 657–684. [[CrossRef](#)]
20. Novotný, P.; Yusuf, S.; Li, F.X.; Lamb, H.H. Oxidative Dehydrogenation of Ethane Using MoO₃/Fe₂O₃ Catalysts in a Cyclic Redox Mode. *Catal. Today* **2018**, *317*, 50–55. [[CrossRef](#)]
21. Zhao, K.; He, F.; Huang, Z.; Wei, G.Q.; Zheng, A.Q.; Liu, H.B.; Zhao, Z.L. Perovskite-type Oxides LaFe_{1-x}Co_xO₃ for Chemical Looping Steam Methane Reforming to Syngas and Hydrogen Co-production. *Appl. Energ.* **2016**, *168*, 193–203. [[CrossRef](#)]
22. Zhao, H.B.; Tian, X.; Ma, J.C.; Su, M.Z.; Wang, B.W.; Mei, D.F. Development of Tailor-made Oxygen Carriers and Reactors for Chemical Looping Processes at Huazhong University of Science & Technology. *Int. J. Greenh. Gas Con.* **2020**, *93*, 102898.
23. Dudek, R.B.; Gao, Y.F.; Zhang, J.S.; Li, F.X. Manganese-containing Redox Catalysts for Selective Hydrogen Combustion under a Cyclic Redox Scheme. *AIChE J.* **2018**, *64*, 3141–3150. [[CrossRef](#)]
24. Yusuf, S.; Neal, L.; Bao, Z.H.; Wu, Z.L.; Li, F.X. Effects of Sodium and Tungsten Promoters on Mg₆MnO₈-Based Core-Shell Redox Catalysts for Chemical Looping—Oxidative Dehydrogenation of Ethane. *ACS Catal.* **2019**, *9*, 3174–3186. [[CrossRef](#)]
25. Gao, Y.F.; Neal, L.M.; Li, F.X. Li-Promoted La_xSr_{2-x}FeO_{4-δ} Core-Shell Redox Catalysts for Oxidative Dehydrogenation of Ethane under a Cyclic Redox Scheme. *ACS Catal.* **2016**, *6*, 7293–7302. [[CrossRef](#)]
26. Tian, Y.; Dudek, R.B.; Westmoreland, P.R.; Li, F.X. Effect of Sodium Tungstate Promoter on the Reduction Kinetics of CaMn_{0.9}Fe_{0.1}O₃ for Chemical Looping-Oxidative Dehydrogenation of Ethane. *Chem. Eng. J.* **2020**, *398*, 125583. [[CrossRef](#)]
27. Yusuf, S.; Neal, L.; Haribal, V.; Lamb, H.H.; Li, F.X. Manganese Silicate Based Redox Catalysts for Greener Ethylene Production via Chemical Looping-Oxidative Dehydrogenation of Ethane. *Appl. Catal. B-Environ.* **2018**, *232*, 77–85. [[CrossRef](#)]
28. Yusuf, S.; Neal, L.M.; Li, F.X. Effect of Promoters on Manganese-Containing Mixed Metal Oxides for Oxidative Dehydrogenation of Ethane via a Cyclic Redox Scheme. *ACS Catal.* **2017**, *7*, 5163–5173. [[CrossRef](#)]

29. Zhang, L.; Xu, W.B.; Wu, J.; Hu, Y.; Huang, C.D.; Zhu, Y.Y.; Tian, M.; Kang, Y.; Pan, X.L.; Su, Y.; et al. Identifying the Role of A-Site Cations in Modulating Oxygen Capacity of Iron-Based Perovskite for Enhanced Chemical Looping Methane-to-Syngas Conversion. *ACS Catal.* **2020**, *10*, 9420–9430. [[CrossRef](#)]
30. Rajkumar, T.; Sapi, A.; Abel, M.; Kiss, J.; Szenti, I.; Baan, K.; Gomez-Perez, J.F.; Kukovecz, A.; Konya, Z. Surface Engineering of CeO₂ Catalysts: Differences Between Solid Solution Based and Interfacially Designed Ce_{1-x}M_xO₂ and MO/CeO₂ (M=Zn, Mn) in CO₂ Hydrogenation Reaction. *Catal. Lett.* **2021**, *151*, 3477–3491. [[CrossRef](#)]
31. Ahmad, J.; Ahmad, U.; Bukhari, S.H. Synthesis and Optical Properties of La_{1-x}Ce_xMnO₃ Studied by Infrared Reflectivity Measurements. *Chin. J. Phys.* **2018**, *56*, 1439–1448. [[CrossRef](#)]
32. Zhang, C.H.; Hua, W.C.; Wang, C.; Guo, Y.L.; Guo, Y.; Lua, G.Z.; Baylet, A.; Giroir-Fendler, A. The Effect of A-site Substitution by Sr, Mg and Ce on the Catalytic Performance of LaMnO₃ Catalysts for the Oxidation of Vinyl Chloride Emission. *Appl. Catal. B-Environ.* **2013**, *134–135*, 310–315. [[CrossRef](#)]
33. Suarez-Vazquez, S.I.; Moreno-Roman, E.J.; Zanella, R.; Cruz-Lopez, A.; Garcıa-Gomez, C.; Nieto-Marquez, A.; Gil, S. Insight into the Surface Reaction Mechanism of Toluene Oxidation over a Composite CeO_x/La_{1-x}Ce_xMnO₃ Catalyst using DRIFTS. *Chem. Eng. Sci.* **2022**, *259*, 117831. [[CrossRef](#)]
34. Yin, X.L.; Wang, S.; Wang, B.Y.; Shen, L.H. Perovskite-type LaMn_{1-x}B_xO_{3+δ} (B = Fe, CO and Ni) as Oxygen Carriers for Chemical Looping Steam Methane Reforming. *Chem. Eng. J.* **2021**, *422*, 128751. [[CrossRef](#)]
35. Wang, Y.J.; Zheng, Y.E.; Wang, Y.H.; Wang, H.; Zhu, X.; Wei, Y.G.; Wang, Y.M.; Jiang, L.H.; Yang, Z.Y.; Li, K.Z. Evaluation of Fe Substitution in Perovskite LaMnO₃ for the Production of High Purity Syngas and Hydrogen. *J. Power Sources* **2020**, *449*, 227505. [[CrossRef](#)]
36. Zhao, K.; He, F.; Huang, Z.; Wei, G.Q.; Zheng, A.Q.; Li, H.B.; Zhao, Z.L. Perovskite-type LaFe_{1-x}Mn_xO₃ (x = 0, 0.3, 0.5, 0.7, 1.0) Oxygen Carriers for Chemical-looping Steam Methane Reforming: Oxidation Activity and Resistance to Carbon Formation. *Korean J. Chem. Eng.* **2017**, *34*, 1651–1660. [[CrossRef](#)]
37. Jiang, S.C.; Ding, W.X.; Zhao, K.; Huang, Z.; Wei, G.Q.; Feng, Y.Y.; Lv, Y.J.; He, F. Enhanced Chemical Looping Oxidative Coupling of Methane by Na-doped LaMnO₃ Redox Catalysts. *Fuel* **2021**, *299*, 120932. [[CrossRef](#)]
38. Ponce, S.; Pena, M.A.; Fierro, J.L.G. Surface Properties and Catalytic Performance in Methane Combustion of Sr-substituted Lanthanum Manganites. *Appl. Catal. B-Environ.* **2000**, *24*, 193–205. [[CrossRef](#)]
39. Zhang, C.H.; Zeng, K.; Wang, C.; Liu, X.H.; Wu, G.L.; Wang, Z.; Wang, D. LaMnO₃ Perovskites via a Facile Nickel Substitution Strategy for Boosting Propane Combustion Performance. *Ceram. Int.* **2020**, *46*, 6652–6662. [[CrossRef](#)]
40. Najjar, H.; Lamonier, J.-F.; Mentre, O.; Giraudon, J.-M.; Batis, H. Optimization of the Combustion Synthesis towards Efficient LaMnO_{3+y} Catalysts in Methane Oxidation. *Appl. Catal. B-Environ.* **2011**, *106*, 149–159. [[CrossRef](#)]
41. Yang, X.Q.; Yu, X.L.; Jing, M.Z.; Song, W.Y.; Liu, J.; Ge, M.F. Defective Mn_xZr_{1-x}O₂ Solid Solution for the Catalytic Oxidation of Toluene: Insights into the Oxygen Vacancy Contribution. *ACS Appl. Mater. Inter.* **2019**, *11*, 730–739. [[CrossRef](#)] [[PubMed](#)]
42. Zhang, C.H.; Wang, C.; Hua, W.H.; Guo, Y.L.; Lu, G.Z.; Gil, S.; Giroir-Fendler, A. Relationship between Catalytic Deactivation and Physicochemical Properties of LaMnO₃ Perovskite Catalyst during Catalytic Oxidation of Vinyl Chloride. *Appl. Catal. B-Environ.* **2016**, *186*, 173–183. [[CrossRef](#)]
43. Zhu, J.J.; Zhao, Z.; Xiao, D.H.; Li, J.; Yang, X.G.; Wu, Y. Study of La_{2-x}Sr_xCuO₄ (x = 0.0, 0.5, 1.0) Catalysts for NO+CO Reaction from the Measurements of O₂-TPD, H₂-TPR and Cyclic Voltammetry. *J. Mol. Catal. A-Chem.* **2005**, *238*, 35–40. [[CrossRef](#)]
44. Wang, T.; Gao, Y.F.; Liu, Y.Z.; Song, M.H.; Liu, J.J.; Guo, Q.J. Core-shell Na₂WO₄/CuMn₂O₄ Oxygen Carrier with High Oxygen Capacity for Chemical Looping Oxidative Dehydrogenation of Ethane. *Fuel* **2021**, *303*, 121286. [[CrossRef](#)]
45. Galinsky, N.; Mishra, A.; Zhang, J.; Li, F.X. Ca_{1-x}A_xMnO₃ (A = Sr and Ba) Perovskite Based Oxygen Carriers for Chemical Looping with Oxygen Uncoupling (CLOU). *Appl. Energ.* **2015**, *157*, 358–367. [[CrossRef](#)]
46. He, F.; Li, X.A.; Zhao, K.; Huang, Z.; Wei, G.Q.; Li, H.B. The Use of La_{1-x}Sr_xFeO₃ Perovskite-type Oxides as Oxygen Carriers in Chemical-looping Reforming of Methane. *Fuel* **2013**, *108*, 465–473. [[CrossRef](#)]
47. Song, D.; Lin, Y.; Zhao, K.; Huang, Z.; He, F.; Xiong, Y. Migration Mechanism of Lattice Oxygen: Conversion of CO₂ to CO Using NiFe₂O₄ Spinel Oxygen Carrier in Chemical Looping Reactions. *Catalysts* **2022**, *12*, 1181. [[CrossRef](#)]
48. Zhang, C.H.; Guo, Y.L.; Guo, J.; Lu, G.Z.; Boreave, A.; Retailleau, L.; Baylet, A.; Giroir-Fendler, A. LaMnO₃ Perovskite Oxides Prepared by Different Methods for Catalytic Oxidation of Toluene. *Appl. Catal. B-Environ.* **2014**, *148–149*, 490–498. [[CrossRef](#)]

Disclaimer/Publisher’s Note: The statements, opinions and data contained in all publications are solely those of the individual author(s) and contributor(s) and not of MDPI and/or the editor(s). MDPI and/or the editor(s) disclaim responsibility for any injury to people or property resulting from any ideas, methods, instructions or products referred to in the content.